ARTICLE OPEN

Controlled-phase gate by dynamic coupling of photons to a two-level emitter

Stefan Krastanov [1✉], Kurt Jacobs [2,3], Gerald Gilbert[4], Dirk R. Englund [1] and Mikkel Heuck[1,5✉]

We propose an architecture for achieving high-fidelity deterministic quantum logic gates on dual-rail encoded photonic qubits by letting photons interact with a two-level emitter (TLE) inside an optical cavity. The photon wave packets that define the qubit are preserved after the interaction due to a quantum control process that actively loads and unloads the photons from the cavity and dynamically alters their effective coupling to the TLE. The controls rely on nonlinear wave mixing between cavity modes enhanced by strong externally modulated electromagnetic fields or on AC Stark shifts of the TLE transition energy. We numerically investigate the effect of imperfections in terms of loss and dephasing of the TLE as well as control field miscalibration. Our results suggest that III-V quantum dots in GaAs membranes is a promising platform for photonic quantum information processing.

INTRODUCTION

In quantum networks, optical photons are the main carrier of quantum information. The absence of direct interaction between photons and their high excitation energy make them immune to the otherwise pervasive thermal noise. Conversely, the lack of direct interaction creates significant challenges to the use of photons as the substrate for quantum computation, where fast, high-fidelity logic gates between the (photonic) qubits are necessary. Effective interactions derived from measurements[1] result in probabilistic gates. Instead, we focus on deterministic gate implementations through coherent photon-photon interactions based on optical nonlinearities. Bulk optical nonlinearities are attractive due to their potential for room-temperature operation[2–6], but their strength remains too weak. At cryogenic temperatures, stronger nonlinearities arise by coupling photons to ancillary quantum systems. For instance, strong interactions between photons and two-level emitters (TLEs) have been realized in many physical systems including atoms[7,8], quantum dots[9,10], molecules[11], superconducting circuits[12], and ions[13]. It is widely accepted that passive TLE systems are insufficient to implement high-fidelity controlled-phase gates[14,15]. Multi-stage approaches including active wave packet control[14,16] increase resource overhead and optical loss. Ancillary qubits based on multi-level atomic systems[17–19] provide added flexibility but at a significant cost in technological complexity. A dynamic cavity control scheme was employed in Refs. [3,4] for bulk nonlinearities, but it remains an open question whether a similar approach works for TLEs. For the $\chi^{(2)}$ and $\chi^{(3)}$ interactions of refs. [3,4] both one- and two-photon cavity states are straightforwardly coupled out once a π-phase difference between them is achieved[3,4]. For TLEs, however, a state with n photons has a Rabi frequency proportional to $\sqrt{n}$ so evacuating the cavity for both $n = 1$ and $n = 2$ is nontrivial.

Here, we introduce a single-stage dynamic control scheme for photonic qubits that exploits the strong interactions with a TLE in a multimode cavity. Figure 1 illustrates how photons traveling in wave packets are actively loaded into a resonator where they interact via the TLE and are subsequently released into the same wave packet with transformed photon-number contents. We assume to have control over the detuning between the TLE and cavity mode $\hat{b}$ such that $\Omega(t) = \omega_e - \omega_b$. This provides control over the effective Rabi frequency $\sqrt{g^2 + \Omega(t)^2/4}$ (see the supplementary materials) to enable both one- and two-photon input states to be coupled out efficiently. We also assume to have control over the coupling between cavity modes $\hat{a}$ and $\hat{b}$ with a rate $\Lambda(t)$. This can be achieved by three-wave-mixing between the aforementioned two modes and a strong controlled classical pump[3,20]. Note that Ref. [21] similarly used two cavity modes coupled by a time-independent rate to improve the trade-off between indistinguishability and efficiency of a quantum emitter.

Since the time-dependent cavity-TLE detuning effectively controls the strength of the nonlinearity, the gate duration can be shortened without reducing the fidelity, in contrast to passive nonlinearities[3,4]. By numerical optimization of $\Omega(t)$ and $\Lambda(t)$, we show that high-fidelity controlled-phase gates are, in fact, possible and further that the gate duration need only exceed the Rabi period at zero-detuning by a factor of 2–3.

This manuscript is organized as follows: In the next section, we derive the general form of the equations of motion for one- and two-photon wave packets incident on the cavity-TLE system. This serves at the basis for our control conditioned on the photon number of the wave packets. These equations are used in the section "Results" to derive control fields that enable a high-fidelity controlled-phase gate as an example of the many logical operations enabled by this design. The section "Discussion" provides a detailed study of the performance of that gate with respect to various hardware parameters. Lastly, we provide an outlook on possible near-term hardware implementations and concluding remarks.

[1]Department of Electrical Engineering and Computer Science, Massachusetts Institute of Technology, 77 Massachusetts Avenue, Cambridge, MA 02139, USA. [2]U.S. Army Research Laboratory, Sensors and Electron Devices Directorate, Adelphi, MD 20783, USA. [3]Department of Physics, University of Massachusetts at Boston, Boston, MA 02125, USA. [4]The MITRE Coorporation, 200 Forrestal Road, Princeton, NJ 08540, USA. [5]Department of Electrical and Photonics Engineering, Technical University of Denmark, 2800 Kgs. Lyngby, Denmark. ✉email: stefankr@mit.edu; mheu@dtu.dk
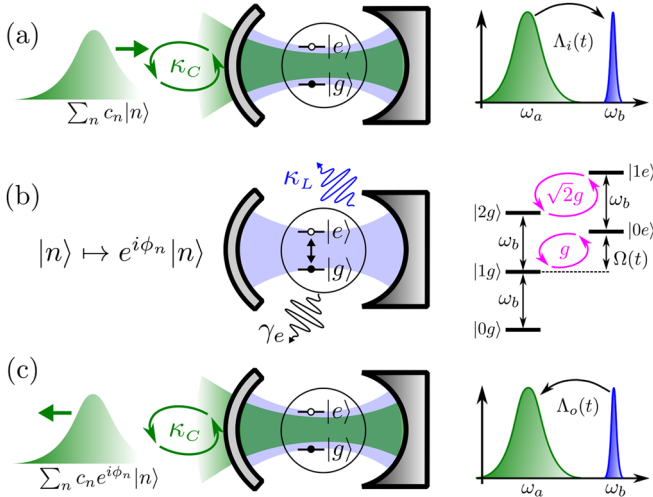
Fig. 1 Schematic representation of the system and steps of the gate protocol. a An incoming wave packet (green) in state $\sum c_n|n\rangle$ is coupled into a cavity mode $\hat{a}$ (also green). Mode $\hat{a}$ is coupled to a second available mode $\hat{b}$ (blue) via an external control field $\Lambda_i(t)$ as depicted in the spectrum diagram on the right. This coupling enables the capture of the incoming ω_a wave packet into mode $\hat{b}$. b Mode $\hat{b}$ is coupled to a two-level emitter (TLE) at vacuum rate g. We control the detuning of the TLE through an external field described by $\Omega(t)$. As seen in the energy-level diagram, the cavity-TLE coupling depends on the number of photons in mode $\hat{b}$, which enables the depicted photon-number-dependent transformation. c Controlled release using a second control pulse, $\Lambda_o(t)$. The state of the outgoing packet has undergone phase changes conditioned on the number of photons.

METHODS

Equations of motion

Before demonstrating the implementation of a controlled-phase gate, we will describe the general form of the dynamics of capturing (and releasing) a wave packet into our two-mode cavities in the presence of a TLE. The TLE is crucial for the non-Gaussian quantum operations we want to perform. We use the discrete-time formalism developed in Ref. [3] to describe the system in Fig. 1. It involves discretizing the time axis into N bins of width Δt and introducing discrete-time waveguide mode operators

$$\hat{w}(t_k) = \hat{w}(k\Delta t) \equiv \frac{\hat{w}_k}{\sqrt{\Delta t}} \quad \text{with} \quad [\hat{w}_j, \hat{w}_k^\dagger] = \delta_{jk}, \tag{1}$$

where $\hat{w}(t_k)$ is the continuous-time annihilation operator of the waveguide mode that couples to cavity mode $\hat{a}$. The input state of a single photon is

$$\left|\psi_{\text{in}}^{(1)}\right\rangle = \int_{t_0}^{t_N} dt\, \xi_{\text{in}}(t)\hat{w}^\dagger(t)|\emptyset\rangle \approx \sum_{k=1}^{N} \sqrt{\Delta t}\, \xi_k^{\text{in}} \hat{w}_k^\dagger|\emptyset\rangle, \tag{2}$$

where $\int_{t_0}^{t_N} |\xi_{\text{in}}(t)|^2 = 1$ so the state is normalized, $\xi_k^{\text{in}} = \xi_{\text{in}}(t_k)$ describes the shape of the wave packet, and $|\emptyset\rangle$ denotes the vacuum state of the waveguide. To each time bin, n, there is an associated Hamiltonian

$$\frac{\hat{H}_n}{\hbar} = \Omega_n \hat{\sigma}_{ee} + i\sqrt{\frac{\kappa_C}{\Delta t}}\left(\hat{a}^\dagger \hat{w}_n - \hat{a}\hat{w}_n^\dagger\right) + \Lambda_n^* \hat{a}^\dagger \hat{b} + \Lambda_n \hat{a}\hat{b}^\dagger + g\left(\hat{b}^\dagger \hat{\sigma}_- + \hat{b}\hat{\sigma}_+\right), \tag{3}$$

which describes the interaction between the cavity and photons in the waveguide at time t_n as well as the internal dynamics of the cavity. The propagation of the wave packet is, thus, handled implicitly (instead of introducing an additional hopping Hamiltonian). The operators describing the TLE in Eq. (3) are $\hat{\sigma}_{ee} = |e\rangle\langle e|$, $\hat{\sigma}_- = |g\rangle\langle e|$, and $\hat{\sigma}_+ = |e\rangle\langle g|$. The coupling rate between cavity mode $\hat{a}$ and the waveguide is κ_C, the controllable coupling between modes $\hat{a}$ and $\hat{b}$ is Λ_n, and the coupling rate between the emitter and photons in mode $\hat{b}$ is g. Note that the Hamiltonian in Eq. (3) corresponds to a rotating frame as described in the supplementary materials. Photons in any time bin only interact with
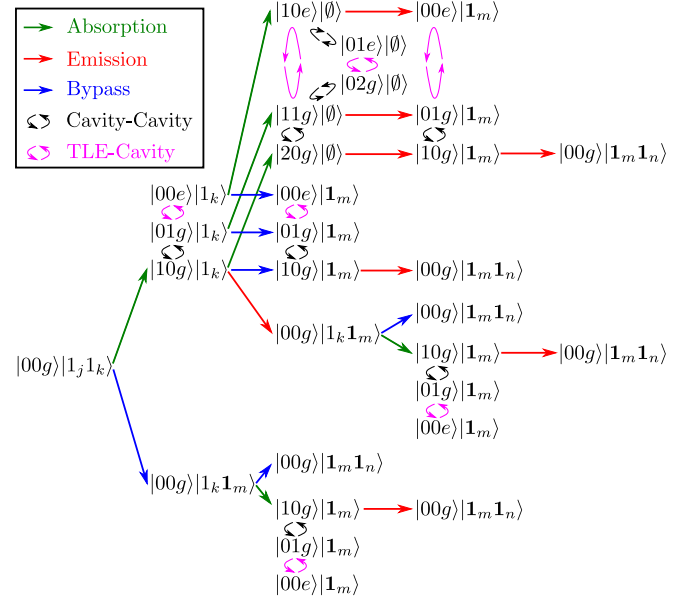
Fig. 2 All input-output paths for two incident photons. Each photon may be absorbed (green) and re-emitted (red) or bypass the cavity by reflecting off of the left mirror in Fig. 1a at time t_m. Inside the cavity, the photons may couple between the cavity modes (black) or between the TLE and mode $\hat{b}$ (magenta).

the cavity once and the bins are ordered such that photons in the first bin interact with the cavity first. At a given time step, t_n, we therefore denote all photons in bins $t_k > t_n$ as *input* photons and write their state as $|1_k\rangle$. Similarly, photons in all bins after the cavity-interaction $t_k \le t_n$ are denoted *output* photons and their state is written in bold as $|\mathbf{1}_k\rangle$. The state of the cavity-TLE system is $|n_a n_b g\rangle$ or $|n_a n_b e\rangle$ when there are n_a photons in mode $\hat{a}$ and n_b photons in mode $\hat{b}$ while the TLE is in the ground, $|g\rangle$, or excited state, $|e\rangle$, respectively.

The flow diagram in Fig. 2 maps out the various paths that two input photons may take while interacting with the system. Each arrow corresponds to a non-zero coupling in the system. We use the diagram as a visual tool to simplify the otherwise tedious job of writing down the dynamical equations. The Schrödinger coefficients corresponding to states with up to two photons remaining on the input side of the cavity at time t are denoted e.g. $\psi_{n_a n_b g}^{(2)}(t)$, where the superscript denotes the maximum number of input photons. As an example, consider the state if the first photon is absorbed into mode $\hat{a}$ and subsequently coupled to mode $\hat{b}$ before the second photon reaches the cavity. The corresponding state is $\psi_{01g}^{(2)}(t)|01g\rangle|1_k\rangle$ with $t_k > t$. States with a maximum of one photon remaining on the input side along with an output photon in bin m have Schrödinger coefficients denoted e.g. $\psi_{n_a n_b g}^{(1)}(t_m, t)$. States with no photons on the input side and an output photon in bin m have coefficients $\psi_{n_a n_b g}^{(0)}(t_m, t)$. Finally, coefficients corresponding to states with both photons in the cavity-TLE system are denoted e.g. $\psi_{n_a n_b g}(t)$ without a superscript.

We refer to Ref. [3] for details of deriving equations of motion for the Schrödinger coefficients, input-output relations, and inclusion of loss channels. For the coefficients mentioned above, describing the state of the cavity in the aforementioned basis, the master equation results in

$$\dot{\psi}_{10g}^{(L)}(t_m, t) = -\frac{\kappa}{2}\psi_{10g}^{(L)}(t_m, t) - i\Lambda(t)^* \psi_{01g}^{(L)}(t_m, t) + \sqrt{L}\sqrt{\kappa_C}\,\xi_{\text{in}}(t) \tag{4a}$$

$$\dot{\psi}_{01g}^{(L)}(t_m, t) = -\frac{\kappa_I}{2}\psi_{01g}^{(L)}(t_m, t) - i\Lambda(t)\psi_{10g}^{(L)}(t_m, t) - ig\psi_{00e}^{(L)}(t_m, t) \tag{4b}$$

$$\dot{\psi}_{00e}^{(L)}(t_m, t) = -\left(i\Omega(t) + \frac{\gamma_e}{2}\right)\psi_{00e}^{(L)}(t_m, t) - ig\psi_{01g}^{(L)}(t_m, t). \tag{4c}$$

The first equation describes the capture of an incoming photon in cavity mode $\hat{a}$ and the interaction between $\hat{a}$ and $\hat{b}$. The latter equations introduce the interaction between mode $\hat{b}$ and the TLE. Note that we included a loss rate, κ_I, for both cavity modes and a decay rate, γ_e, from

the TLE to the electromagnetic environment. The total intensity decay rate from cavity mode $\hat{a}$ is $\kappa = \kappa_C + \kappa_I$ in Eq. (4a) and $L = (0, 1, 2)$ is the maximum number of photons on the input side as described above. Note that solving Eq. (4) with $L = 1$ and $t_m = 0$ corresponds to a one-photon input state.

The Schrödinger coefficients corresponding to both photons being in the TLE-cavity system evolve according to

$$\dot{\psi}_{20g}(t) = -\kappa\psi_{20g}(t) - i\sqrt{2}\Lambda(t)^*\psi_{11g}(t) + \sqrt{2\kappa_C}\psi_{10g}^{(2)}(t)\xi_{in}(t) \tag{5a}$$

$$\dot{\psi}_{11g}(t) = -\frac{\kappa_C + 2\kappa_I}{2}\psi_{11g}(t) - i\sqrt{2}[\Lambda(t)\psi_{20g}(t) + \Lambda(t)^*\psi_{02g}(t)] - ig\psi_{10e}(t) + \sqrt{\kappa_C}\psi_{01g}^{(2)}(t)\xi_{in}(t) \tag{5b}$$

$$\dot{\psi}_{02g}(t) = -\kappa_I\psi_{02g}(t) - i\sqrt{2}\Lambda(t)\psi_{11g}(t) - i\sqrt{2}g\psi_{01e}(t) \tag{5c}$$

$$\dot{\psi}_{10e}(t) = -\left(i\Omega(t) + \frac{\gamma_e + \kappa}{2}\right)\psi_{10e}(t) - i\Lambda(t)^*\psi_{01e}(t) - ig\psi_{11g}(t) + \sqrt{\kappa_C}\psi_{00e}^{(2)}(t)\xi_{in}(t) \tag{5d}$$

$$\dot{\psi}_{01e}(t) = -\left(i\Omega(t) + \frac{\gamma_e}{2} + \frac{\kappa_I}{2}\right)\psi_{01e}(t) - i\Lambda(t)\psi_{10e}(t) - i\sqrt{2}g\psi_{02g}(t). \tag{5e}$$

The initial condition for Eq. (5) is that all coefficients are zero at $t = t_0$. Note that all driving terms in Eqs. (4) and (5) correspond to green arrows in Fig. 2 while all terms proportional to Λ and g correspond to black and magenta arrows, respectively. As such, Fig. 2 provides a convenient tool for verifying that all interactions are included in the dynamical equations.

For $L = 2$ in Eq. (4), the only required initial condition is $\psi_{10g}^{(2)}(0) = \psi_{01g}^{(2)}(0) = \psi_{00e}^{(2)}(0) = 0$. Those coefficients are therefore only functions of a single variable, t. For $L = 1$ and $L = 0$, the equations must be solved for N different initial conditions since t_m corresponds to any bin and the coefficients are functions of both t_m and $t \geq t_m$.

For $L = 1$, the dynamics is initiated by either an emission into the waveguide or simply a bypass (the traveling photon passing by the cavity)

$$|10g\rangle|1_k\rangle \rightarrow |00g\rangle|1_k\mathbf{1}_m\rangle \tag{6a}$$

$$|00g\rangle|1_j1_k\rangle \rightarrow |00g\rangle|1_k\mathbf{1}_m\rangle. \tag{6b}$$

In either case, the initial conditions are: $\psi_{10g}^{(1)}(t_m, t_m) = \psi_{01g}^{(1)}(t_m, t_m) = \psi_{00e}^{(1)}(t_m, t_m) = 0$.

For $L = 0$, the dynamics is initiated by one of three different emission paths or three different bypass paths

$$|10e\rangle|\emptyset\rangle \rightarrow |00e\rangle|\mathbf{1}_m\rangle \tag{7a}$$

$$|11g\rangle|\emptyset\rangle \rightarrow |01g\rangle|\mathbf{1}_m\rangle \tag{7b}$$

$$|20g\rangle|\emptyset\rangle \rightarrow |10g\rangle|\mathbf{1}_m\rangle \tag{7c}$$

$$|00e\rangle|1_k\rangle \rightarrow |00e\rangle|\mathbf{1}_m\rangle \tag{7d}$$

$$|01g\rangle|1_k\rangle \rightarrow |01g\rangle|\mathbf{1}_m\rangle \tag{7e}$$

$$|10g\rangle|1_k\rangle \rightarrow |10g\rangle|\mathbf{1}_m\rangle. \tag{7f}$$

To understand how to set the initial conditions of Eq. (4) with $L = 0$ based on the events listed in Eq. (7), we consider the entire paths through the map in Fig. 2. As an example, we consider the top path, which Eq. (7a) is a part of

$$|00g\rangle|1_j1_k\rangle \rightarrow |10g\rangle|1_k\rangle \rightarrow |10e\rangle|\emptyset\rangle \rightarrow -\sqrt{\kappa_C\Delta t}\psi_{10e}(t_m)|00e\rangle|\mathbf{1}_m\rangle \rightarrow -\sqrt{\kappa_C\Delta t}\psi_{10g}^{(0)}(t_m, t_n)|00g\rangle|\mathbf{1}_m\mathbf{1}_n\rangle. \tag{8}$$

At each emission or bypass event, we explicitly write out the coefficient of the relevant state and the initial condition of Eq. (4) is therefore $\psi_{00e}^{(0)}(t_m, t_m) = -\sqrt{\kappa_C\Delta t}\psi_{10e}(t_m)$, while the other coefficients are initialized with the value zero. However, since Eq. (4) is linear, we may use the initial value 1 and multiply the contributions to the output state in the end, such that the contribution from the path in Eq. (8) is $\kappa_C\psi_{10e}(t_m)\psi_{10g}^{(0)}(t_m, t_n)$. To distinguish between which of the three coefficients $\psi_{00e}^{(0)}$, $\psi_{01g}^{(0)}$, or $\psi_{10g}^{(0)}$ that is initialized to 1, we define functions $\{A_{00e}, A_{01g}, A_{10g}\}$, $\{B_{00e}, B_{01g}, B_{10g}\}$, and $\{C_{00e}, C_{01g}, C_{10g}\}$, where A corresponds to $\psi_{10g}^{(0)}(t_m, t_m) = 1$, B to
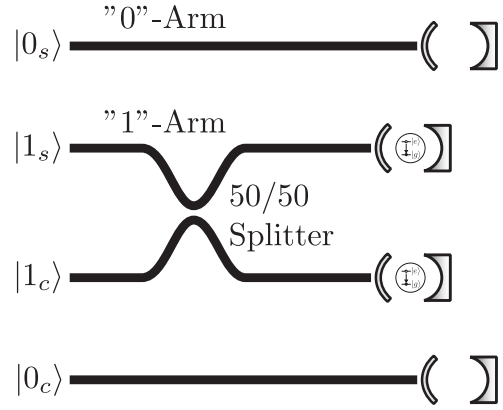

Fig. 3 Photonic integrated circuit implementation of a controlled-phase gate. The gate acts on two dual-rail qubits encoded in four waveguides. The top two waveguides serve to encode one qubit. The logical state of that qubit depends on which of the waveguides contains a photon, as labeled on their left end. All four waveguides are terminated by identical one-sided cavities depicted in Fig. 1a. The "0"-arm cavities preserve the relative timing of the photon pulses and need not contain TLEs. The "1"-arm cavities perform the nonlinear phase shift and must contain identical TLEs. A 50/50 beamsplitter between the "1"-arms cause the transformation $|1_w1_w\rangle \rightarrow 1/\sqrt{2}(|2_w0_w\rangle + |0_w2_w\rangle)$ resulting in two photons arriving at one of the TLE cavities if the logical state of the qubits is $|11\rangle$ (i.e., a photon in each of the middle two waveguides.). The cavity control is such that they map $|1_w\rangle \mapsto |1_w\rangle$, but $|2_w\rangle \mapsto -|2_w\rangle$. This extra phase is the crucial component enabling our controlled-phase gate. We use the w subscript to denote physical photon in a waveguide, to avoid confusion with the notation used for the logical states of the dual-rail qubits.

$\psi_{01g}^{(0)}(t_m, t_m) = 1$, and C to $\psi_{00e}^{(0)}(t_m, t_m) = 1$. Following all the paths in Fig. 2, the output state is found to consist of the following ten terms

$$\xi_{out}^{(2)}(t_m, t_n) = \frac{\kappa_C}{\sqrt{2}}\left[\psi_{10e}(t_m)C_{10}(t_m, t_n) + \psi_{11g}(t_m)B_{10}(t_m, t_n) + \sqrt{2}\psi_{20g}(t_m)A_{10}(t_m, t_n)\right.$$
$$- \frac{\xi_{in}(t_m)}{\sqrt{\kappa_C}}\left(\psi_{00e}^{(2)}(t_m)C_{10}(t_m, t_n) + \psi_{01g}^{(2)}(t_m)B_{10}(t_m, t_n) + \psi_{10}^{(2)}(t_m)A_{10}(t_m, t_n)\right)$$
$$\left. - \frac{\psi_{10g}^{(2)}(t_m)}{\sqrt{\kappa_C}}\left(\xi_{in}(t_n) - \sqrt{\kappa_C}\psi_{10g}^{(1)}(t_m, t_n)\right) + \sqrt{2}\xi_{in}(t_m)\left(\xi_{in}(t_n) - \sqrt{\kappa_C}\psi_{10g}^{(1)}(t_m, t_n)\right)\right], \tag{9a}$$

where $t_m \leq t_n$. The output state for two-photon inputs is

$$\left|\psi_{out}^{(2)}\right\rangle = \int_{t_0}^{t_N}\int_{t_0}^{t_N}dt_m dt_n \xi_{out}^{(2)}(t_m, t_n)\hat{w}^\dagger(t_m)\hat{w}^\dagger(t_n)|\emptyset\rangle. \tag{10}$$

The input-output relation for one-photon inputs is found by considering the two paths starting from the state $|00g\rangle|1_k\mathbf{1}_m\rangle$, which may be considered the single-photon branch of the map in Fig. 2. The result is

$$\xi_{out}^{(1)}(t) = \xi_{in}(t) - \sqrt{\kappa_C}\psi_{10g}^{(1)}(t), \tag{11}$$

with a single-photon output state given by

$$\left|\psi_{out}^{(1)}\right\rangle = \int_{t_0}^{t_N}dt\,\xi_{out}^{(1)}(t)\hat{w}^\dagger(t)|\emptyset\rangle. \tag{12}$$

Controlled-phase gate

Having presented the equations governing the general time-evolution of an input state in product form, we turn to the specific example of implementing a controlled-phase gate on two dual-rail encoded photonic qubits. Other quantum logic operations are in principle possible as well, but the controlled-phase gate is a prototypical example of a low-level two-qubit operation. Together with the available continuous single-qubit gates it completes the requirements for universal quantum circuits. Figure 3 sketches the envisioned photonic integrated circuit implementation. The basic idea is that we arrange our TLE-cavity systems to act as an identity operation on incoming single-

photon wave packets (or the vacuum), while at the same time they impart a nontrivial phase to a two-photon wave packet. The dual rail encoding and the beamsplitter ensure that the cavities encounter two-photon wave packets only for the logical $|11\rangle$ state, leading to our controlled-phase operation.

The input state (two arbitrary dual-rail encoded qubits) is[15]

$$|\psi_{sc}\rangle = (a|0_s\rangle + \beta|1_s\rangle) \otimes (\zeta|0_c\rangle + \vartheta|1_c\rangle) \equiv a\zeta|00\rangle + a\vartheta|01\rangle + \beta\zeta|10\rangle + \beta\vartheta|11\rangle, \quad (13)$$

with $|a|^2 + |\beta|^2 = 1$ and $|\zeta|^2 + |\vartheta|^2 = 1$. The ideal controlled-phase gate operation is defined by the transformation

$$\hat{C}|\psi_{sc}\rangle \equiv a\zeta|00\rangle + a\vartheta|01\rangle + \beta\zeta|10\rangle - \beta\vartheta|11\rangle. \quad (14)$$

We use the "worst-case" gate fidelity as defined in[22]

$$\mathcal{F}_{gate} \equiv \min_{|\psi_{sc}\rangle}(\mathcal{F}_s), \quad (15)$$

where the state fidelity, $\mathcal{F}_s$, is defined as

$$\mathcal{F}_s \equiv \left|\langle\psi_{sc}|\hat{C}^\dagger|\psi_{out}\rangle\right|^2 = \left|(|a|^2 + |\beta\zeta|^2)\langle 1_w|\psi_{out}^{(1)}\rangle^2 - |\beta\vartheta|^2\langle 2_w|\psi_{out}^{(2)}\rangle\right|^2, \quad (16)$$

where $|1_w\rangle$ and $|2_w\rangle$ denote, respectively, one or two photons in the waveguide and $\left|\psi_{out}^{(1)}\right\rangle$ and $\left|\psi_{out}^{(2)}\right\rangle$ denote the emitted state after the absorption of, respectively, one or two incident photons. We use the w subscript to avoid confusion with the dual-rail logical states, like $|1\rangle = |0_w 1_w\rangle$ and $|0\rangle = |1_w 0_w\rangle$. The steps in the derivation of Eq. (16) are included in the supplementary materials. Notice the minus sign in the second term, corresponding to the fact that the logical $|11\rangle$ state has changed its phase, i.e., that when two photons are absorbed the state gains an additional π phase, unlike when one or zero photons are absorbed. The complex-valued overlap factors in Eq. (16) are given by[4]

$$\langle 1_w|\psi_{out}^{(1)}\rangle = \int \xi_{out}^{(1)}(t)\xi_{in}^*(t - T)dt \quad (17a)$$

$$\langle 2_w|\psi_{out}^{(2)}\rangle = \int\int \xi_{out}^{(2)}(t_m, t_n)\xi_{in}^*(t_n - T)\xi_{in}^*(t_m - T)dt_n dt_m, \quad (17b)$$

where T is the gate duration. Note that the output wave packet of the ideal gate operation is a simple time translation of the input wave packet. This is a critical requirement for enabling quantum circuits with many identical gates, as any subsequent gate would work only if the wave packets carrying the encoded photons are not distorted by the previous gate. The output wave packets described by $\xi_{out}^{(1)}$ and $\xi_{out}^{(2)}$ are not normalized due to loss and $|\psi_{00e}(t_N)|^2 \geq 0$. The overlap integrals in Eq. (17) therefore describes gate errors in both amplitude and phase.

For the system considered here, the task is to determine the control fields $\Lambda(t)$ (the interaction between the cavity modes) and $\Omega(t)$ (the detuning between the TLE and cavity mode $\hat{b}$) that maximize the gate fidelity. Unity fidelity is achieved if $\langle 1_w|\psi_{out}^{(1)}\rangle = 1$ and $\langle 2_w|\psi_{out}^{(2)}\rangle = -1$ as seen from Eq. (16). This means that a two-photon wave packet captured and then released by the cavity must acquire a different phase than that of a single photon to fulfill the condition $\arg[\xi_{out}^{(2)}] - 2\arg[\xi_{out}^{(1)}] = \pi$. The photon-number dependent TLE-cavity coupling illustrated in Fig. 1 causes an an-harmonic energy-ladder that enables this difference in phase-accumulation. However, in Refs. [3,4] we found that the gate fidelity is limited due to interactions between the photons while the wave packet is absorbed and released from the cavity. This fidelity reduction would be particularly detrimental with the large nonlinearity considered here without a method to modify the effective size of the nonlinear coupling rate. Instead of changing g itself, we consider modifying the TLE-cavity detuning, $\Omega(t)$. When $\Omega \gg g$, the effective nonlinearity is small and it is maximized when $\Omega = 0$. The gate protocol therefore consists of three stages:

Absorption: $\Lambda(t)$ is adjusted to couple photons from an incident wave packet into mode $\hat{b}$ while the detuning is held fixed at a large value $\Omega(t) = \Omega_0 \gg g$.
Interaction: $\Omega(t)$ is adjusted to increase the effective nonlinear coupling rate such that the required phase shift is achieved while the TLE returns to its ground state at the end of the stage for both one- and two-photon inputs.
Emission: $\Lambda(t)$ is turned on again to release the photons into a wave packet with the same shape as the input while $\Omega(t) = \Omega_0$.

When the TLE and cavity are completely decoupled, the optimum control function that loads a single photon into mode $\hat{b}$ is [3]

$$|\Lambda_i(t)| = \frac{|f_i|\exp\left[-\frac{\kappa_l t}{2}\right]}{|\xi_{in}|\sqrt{2\int_{t_0}^t f_i(s)ds}} \quad (18a)$$

$$\arg[\Lambda_i(t)] = -\delta_b t - \arg(\xi_{in}), \quad (18b)$$

$$f_i(t) = \left(\frac{\kappa_C}{2}\xi_{in} - \dot{\xi}_{in}\right)\xi_{in}^* e^{\kappa_l t}, \quad (18c)$$

where $\delta_b = 0$ and we assumed $\Lambda_i(t)$ arises due to three-wave mixing between modes $\hat{a}$, $\hat{b}$, and a third mode [not shown in Fig. 1(a)] occupied by a strong classical laser field. In the limit $\Omega_0 \gg g$, we can adiabatically eliminate $\psi_{00e}^{(L)}$ from Eq. (4b) by setting $\dot{\psi}_{00e}^{(L)} \approx 0$ in Eq. (4c), leading to

$$\dot{\psi}_{01g}^{(L)}(t_m, t) \approx \left(-\frac{\kappa_l}{2} + i\frac{g^2}{\Omega_0}\right)\psi_{01g}^{(L)}(t_m, t) - i\Lambda(t)\psi_{10g}^{(L)}(t_m, t) \quad (19a)$$

$$\dot{\psi}_{00e}^{(L)}(t_m, t) \approx -\frac{g}{\Omega_0}\psi_{01g}^{(L)}(t_m, t). \quad (19b)$$

The term g^2/Ω_0 therefore corresponds to adding an effective detuning in Eq. (4b) so we add $g^2/\Omega_0 t$ to the phase of $\Lambda_i(t)$ when solving for the full dynamics described by Eq. (4). An alternative derivation of this additional phase term is found in the supplementary materials.

The control function that optimally releases a single photon into the wave packet ξ_{out}, is[3]

$$|\Lambda_o(t)| = \frac{|f_o|e^{-\frac{\kappa_l t}{2}}}{|\xi_{out}|\sqrt{\kappa_C|\psi_{01}^{(1)}(t_0)|^2 - 2\int_{t_0}^t f_o(s)ds}} \quad (20a)$$

$$\arg[\Lambda_o(t)] = -\delta_b t - \arg(\xi_{out}) - \frac{\pi}{2} \quad (20b)$$

$$f_o(t) = \left(\frac{\kappa_C}{2}\xi_{out} + \dot{\xi}_{out}\right)\xi_{out}^* e^{\kappa_l t}. \quad (20c)$$

Note there is some additional optimization involved when $\psi_{01g}^{(1)}(0, t)$ has not reached a steady-state value at the onset of the release process since it is not obvious how to chose $\psi_{01g}^{(1)}(t_0)$ in Eq. (20a). Since both Λ_i and Λ_o are approximately zero during the interaction stage, we have $\Lambda = \Lambda_i + \Lambda_o$.

RESULTS

Gate performance

To quantify the gate performance that is possible with the system in Figs. 1, 3, we consider Gaussian-envelope wave packets

$$\xi_{in}(t) = \sqrt{\frac{2}{\tau_\mathcal{G}}}\left(\frac{\ln(2)}{\pi}\right)^{\frac{1}{4}}\exp\left(-2\ln(2)\frac{(t - T_{in})^2}{\tau_\mathcal{G}^2}\right), \quad (21)$$

where $|\xi_{in}(t)|^2$ has a full temporal width at half maximum (FWHM) of $\tau_\mathcal{G}$ and a spectral width of $\Omega_\mathcal{G} = 4\ln(2)/\tau_\mathcal{G}$. We numerically solved the equations in the section "Equations of motion" using `Julia`[23]. The temporal shape of the control field $\Omega(t)$ was determined by minimizing the gate error $1 - \mathcal{F}_{gate}$ using a standard gradient-free optimization method (Nelder–Mead[24]). Figure 4 shows an example of the gate dynamics for a duration of $T = 7/g$, $T_{in} = 4.3/g$, and $g = 0.4\Omega_\mathcal{G}$. It is expected that the TLE-cavity detuning becomes small during the interaction stage, $t \in [T_{in}; T_{in} + T]$, since it leads to a larger occupation probability of the TLE and thereby a larger effective nonlinearity. The blue curve in Fig. 4a confirms this expectation and Fig. 4b plots the probability of the TLE being in the excited state for both one- (blue) and two-photon (red) input states. Note that both populations decrease towards zero at the end of the gate sequence as is required for a large gate fidelity. While the TLE-cavity detuning is low, the one- and two-photon states acquire phase at different rates, which is discussed in more detail in the supplementary materials. Figure 4c plots the phase difference

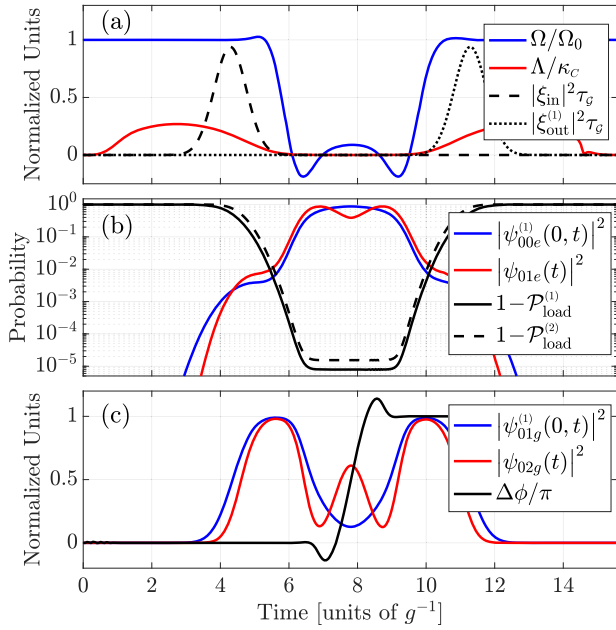$$\Delta\phi(t) \equiv \arg\left[\psi_{02g}(t)\right] - 2\arg\left[\psi_{01g}^{(1)}(0, t)\right], \quad (22)$$

Fig. 4 Example of gate dynamics. a Control functions, $\Lambda(t)$ and $\Omega(t)$ as a function of time along with the input wave packet and ideal one-photon output wave packet, $\xi_{out}^{(1)}$. **b** Probability amplitude of the TLE being excited for a one-photon input, $\psi_{00e}^{(1)}(0,t)$, and the probability amplitude of a photon in mode $\hat{b}$ and an excited TLE for a two-photon input, $\psi_{01e}(t)$. The black curves plot the probability of having absorbed all the input photons [defined in Eq. (23)] for a one- (solid) and two-photon input state (dashed). **c** Probability that all input photons are in mode $\hat{b}$ for a one- (blue) and two-photon input state (red) along with the phase difference between the amplitudes of the corresponding Schrödinger coefficients [defined in Eq. (22)] (black). Simulation parameters: $\kappa_C = 6\Omega_G$, $\kappa_l = \gamma_e = 0$, $g = 0.4\Omega_G$, $\Omega_0 = 15g$, $T_{in} = 4.3/g$, and $T = 7/g$.
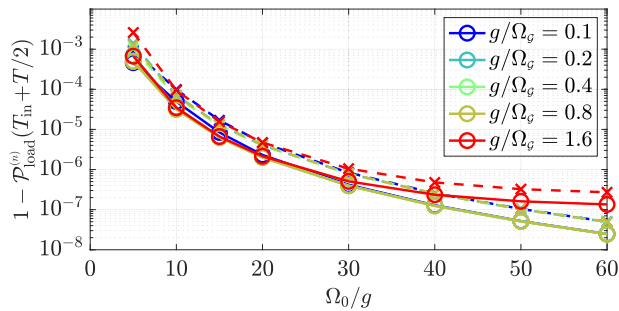

Fig. 5 Probability of failing at photon absorption. Probability not absorbing one- (solid lines) and two-photon (dashed lines) input states as a function the TLE-cavity detuning for different values of g/Ω_G. Simulation parameters: $\kappa_C = 6\Omega_G$, $\kappa_l = \gamma_e = 0$, $T_{in} = 4.3/g$, and $T = 7/g$.

which approximates the phase difference between the output wave packets, $\arg[\xi_{out}^{(2)}] - 2\arg[\xi_{out}^{(1)}]$. The reason is that the populations $|\psi_{02g}(t)|^2$ and $|\psi_{01g}^{(1)}(0,t)|^2$ approach one immediately before the emission stage as seen from Fig. 4c.

The limitation on gate fidelity imposed by a finite value of Ω_0/g is observed in Fig. 4b as a finite absorption probability (black lines). In Fig. 5, we investigate this further by plotting the probability of not absorbing a one- or two-photon input state as a

function of Ω_0/g. The probabilities are given by

$$\mathcal{P}_{load}^{(1)}(t) = \left|\psi_{01g}^{(1)}(0,t)\right|^2 + \left|\psi_{00e}^{(1)}(0,t)\right|^2 \tag{23a}$$

$$\mathcal{P}_{load}^{(2)}(t) = \left|\psi_{02g}(t)\right|^2 + \left|\psi_{01e}(t)\right|^2. \tag{23b}$$

The solution for the phase of the control function, $\Lambda(t)$, uses the term $g^2/\Omega_0 t$ derived in Eq. (19) based on the approximation $\Omega_0 \gg g$. Figure 5 shows how the error probability increases as this approximation becomes worse for decreasing Ω_0/g. Remarkably, the error for both one- and two-photon input states decreases rapidly with increasing Ω_0/g and drops to about 10^{-5} for $\Omega_0 = 15g$.

Our model includes a finite lifetime of cavity modes $\hat{a}$ and $\hat{b}$ as well as a decay rate from the TLE into the electromagnetic environment. Figure 6(a) plots the gate error as a function of gate duration for different values of the loss rate, κ_l. Note that we assumed $\gamma_e = \kappa_l$ in Fig. 6(a). The control function, $\Omega(t)$, was optimized for each parameter configuration. The black line in Fig. 6(a) sets a lower limit on the gate error due to a finite excitation probability of the TLE at t_N as well as a finite absorption error, $1 - \mathcal{P}_{load}$. Compared to Ref. [3], our analysis here studies all three stages of the gate sequence and the gate duration is more than three times shorter (when comparing Fig. 6a here to Fig. 9 in Ref. [3]). The dashed lines in Fig. 6a correspond to the conditional fidelity[3,4], which is calculated using normalized output states

$$\left|\overline{\psi}_{out}^{(n)}\right\rangle \equiv \frac{\left|\psi_{out}^{(n)}\right\rangle}{\sqrt{\langle\psi_{out}^{(n)}|\psi_{out}^{(n)}\rangle}}, \quad n = \{1,2\}. \tag{24}$$

It therefore corresponds to a post-selected gate fidelity conditioned on both photons being detected by a perfect detector. As expected, the conditional fidelity coincides with the fidelity in the absence of loss as in the case of $\chi^{(2)}$ and $\chi^{(3)}$ nonlinearities[4].

Introducing control of the TLE-cavity detuning, $\Omega(t)$, removes the requirement observed in Ref. [4] to increase the gate duration, T, relative to the wave packet width, τ_G, in order to decrease the gate error due to wave packet distortions. Instead, $\Omega(t)$ controls the effective nonlinear coupling and the gate error (in the absence of loss) is only limited by the off-state detuning, Ω_0/g, and the efficiency of depopulating the TLE for both one- and two-photon inputs despite the difference in Rabi frequency.

Working with solid state quantum emitters introduces other types of error mechanisms in addition to loss. Energy-conserving interactions between the emitter and its environment may lead to dephasing, which means the coherence between the ground and excited state is lost[25]. Superposition states, $a|g\rangle + \beta|e\rangle$, turn into mixed states when the relative phase between a and β is not conserved. Here, we study this effect by introducing a dephasing rate, γ_{dp}, and perform Monte-Carlo simulations to calculate the fidelity as described in the supplementary materials following[26,27]. Figure 6b plots the gate error as a function of gate duration for different values of γ_{dp} while keeping $\kappa_l = \gamma_e = 0$.

The result is very similar to that in Fig. 6a, except the dashed and solid lines coincide in Fig. 6(b). Dephasing errors can therefore be considered more severe than loss errors because the post-selected gate fidelity is also affected by dephasing.

Noise in the control fields

In this section, we consider a particular experimental approach to synthesizing the control fields and investigate the effect of noise in the settings of control parameters for $\Omega(t)$. A detuning between the emitter and cavity mode $\hat{b}$ could be controlled via the emitter transition energy, ω_e, through AC-Stark shifts. An alternative scheme would be to modulate the cavity resonance,
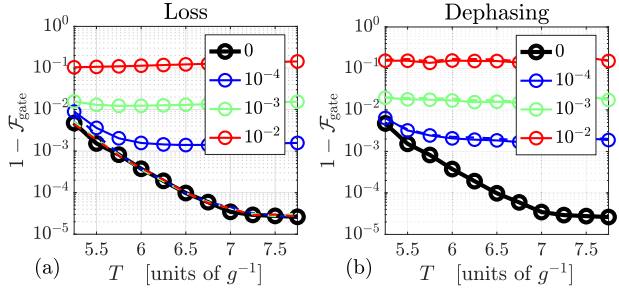
Fig. 6 Dependence of the gate error on decoherence. a $1 - \mathcal{F}_{\text{gate}}$ as a function of gate duration, T, for different cavity loss rates (legend corresponds to κ_l/g). **b** $1 - \mathcal{F}_{\text{gate}}$ as a function of gate duration, T, for different dephasing rates (legend corresponds to γ_{dp}/g). In both (**a**) and (**b**), the dashed lines plot the error in conditional fidelity. Simulation parameters: $\kappa_C = 6\Omega_{\mathcal{G}}$, $g = 0.4\Omega_{\mathcal{G}}$, $\Omega_0 = 15g$, and $T_{\text{in}} = 4.3/g$. In (**a**) we used $\gamma_{\text{dp}} = 0$ and $\gamma_e = \kappa_l \neq 0$ and in (**b**) we used $\gamma_e = \kappa_l = 0$ and $\gamma_{\text{dp}} \neq 0$.

ω_b, via e.g. cross-phase modulation. For experimentally demonstrated nonlinear coupling rates of $g \sim 40$ GHz[28], the entire gate duration in Fig. 4 is $T \sim 175$ ps, which would require very fast electronics. On the other hand, femtosecond-scale resolution in shaping of optical pulses was demonstrated[29]. Typically, optical pulse shaping is achieved by modifying a finite number of Fourier components of pulses using gratings and spatial light modulators[30]. To emulate this process, we write the control field as a sum of super-Gaussians with complex amplitudes in the Fourier domain

$$\tilde{\Omega}(\omega) = \Omega_0 \delta(\omega) - e^{-i\omega T_\Omega} \sum_{m=-\mathcal{N}}^{\mathcal{N}} \tilde{\Omega}^{(m)} e^{-\left(\frac{\omega - m\Omega_{\text{ch}}}{\Omega_{\text{ch}}}\right)^6}, \quad (25)$$

where $\delta(\omega)$ is the Dirac-delta distribution, $\mathcal{N} = (N_{\text{ch}} - 1)/2$, and T_Ω shifts $\Omega(t)$ on the time axis. The number of Fourier components is N_{ch} each having a bandwidth of Ω_{ch}. Since $\Omega(t)$ is real-valued, the optimization consists of determining T_Ω along with $\tilde{\Omega}_R^{(m)} = \text{Re}\{\tilde{\Omega}^{(m)}\}$ and $\tilde{\Omega}_I^{(m)} = \text{Im}\{\tilde{\Omega}^{(m)}\}$ under the constraints $\tilde{\Omega}_R^{(m)} = \tilde{\Omega}_R^{(-m)}$ and $\tilde{\Omega}_I^{(m)} = -\tilde{\Omega}_I^{(-m)}$. Figure 7 shows an example of an optimized control pulse that results in a gate performance similar to the control pulse in Fig. 4a. To see how the gate performance is affected by the number of Fourier components and the channel bandwidth, we plot the minimized gate error as a function of N_{ch} and Ω_{ch} in Fig. 8a.

Experimentally, there is only a finite precision available to determine the shape of the control fields. The Fourier domain implementation enables a direct quantification of the effect on the gate error from noise in the complex amplitudes, $\tilde{\Omega}^{(m)}$, of a programmable filter. The noise is included by modifying the optimized real and imaginary control variables as

$$\tilde{\Omega}_{R/I}^{(m)} \rightarrow \tilde{\Omega}_{R/I}^{(m)} + X_{R/I}^{(m)} \times \sigma \times \max_m\left(\tilde{\Omega}_R^{(m)}, \tilde{\Omega}_I^{(m)}\right). \quad (26)$$

The size of the noise is represented by σ, $X_{R/I}^{(m)}$ is a random number between -1 and 1, and the last factor in Eq. (26) is the maximum of all the optimized variables. Using the maximum in Eq. (26) is motivated by a finite filter setting precision and represents an absolute error rather than a relative error. Adding noise degrades the gate fidelity and Fig. 8b plots the gate error as a function of σ using the same optimized parameters as in Fig. 7. It is observed that errors below 10^{-4} are required to have a negligible influence on the gate error.
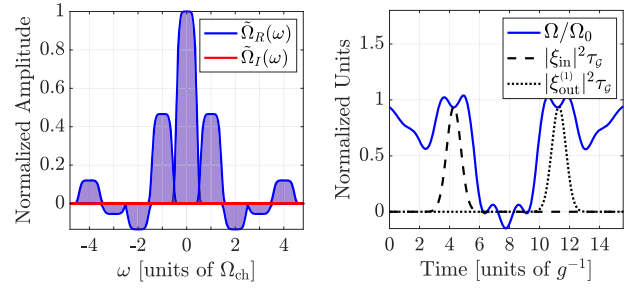

Fig. 7 Example of Fourier domain control function. This particular example leads to a gate error of $1 - \mathcal{F}_{\text{gate}} = 4.7 \times 10^{-5}$. Parameters: $\kappa_C = 6\Omega_{\mathcal{G}}$, $\gamma_e = \kappa_l = 0$, $g = 0.4\Omega_{\mathcal{G}}$, $\Omega_0 = 15g$, $T = 7/g$, $T_{\text{in}} = 4.3/g$, $N_{\text{ch}} = 9$, and $\Omega_{\text{ch}}/g = 0.14$.
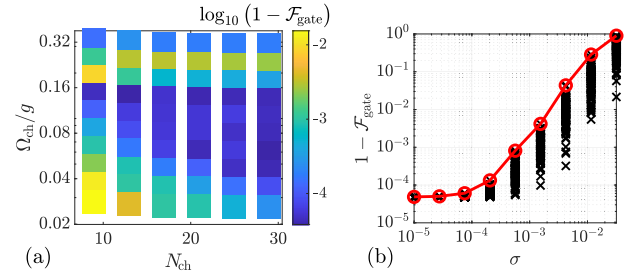

Fig. 8 Gate error as a function of control and hardware parameters. a Optimized gate error, $1 - \mathcal{F}_{\text{gate}}$, as a function of the number of Fourier components, N_{ch}, and their bandwidth, Ω_{ch}. **b** Gate error as a function of the noise parameter, σ, using 100 different combinations of random numbers, $X_{R/I}^{(m)}$, (black crosses). The red line shows the worst case scenario. Parameters: $\kappa_C = 6\Omega_{\mathcal{G}}$, $\gamma_e = \kappa_l = 0$, $g = 0.4\Omega_{\mathcal{G}}$, $\Omega_0 = 15g$, and $T_{\text{in}} = 4.3/g$.

Comparison of nonlinearities

The nonlinearity required to facilitate photon-photon interactions for deterministic quantum logic gates can have different origins. In Refs. [3,4], we proposed protocols based on bulk nonlinearities such as second-harmonic generation (SHG) or self-phase modulation (SPM) in $\chi^{(2)}$ and $\chi^{(3)}$ materials. By introducing a generalized nonlinear coupling rate, Γ_{NL}, we may write the Hamiltonian describing three different nonlinear effects as[3,4]

$$\hat{H}_{\text{SHG}} = \hbar\Gamma_{\text{NL}}\left(\hat{c}\hat{b}^\dagger\hat{b}^\dagger + \hat{c}^\dagger\hat{b}\hat{b}\right) \quad (27a)$$

$$\hat{H}_{\text{SPM}} = \hbar\Gamma_{\text{NL}}\left(\hat{b}^\dagger\hat{b} - 1\right)\hat{b}^\dagger\hat{b} \quad (27b)$$

$$\hat{H}_{\text{TLE}} = \hbar\Gamma_{\text{NL}}\left(\hat{b}^\dagger\hat{\sigma}_- + \hat{b}\hat{\sigma}_+\right). \quad (27c)$$

In Eq. (27a), $\Gamma_{\text{NL}} \propto \chi^{(2)}$, in Eq. (27b), $\Gamma_{\text{NL}} \propto \chi^{(3)}$, and in Eq. (27c), $\Gamma_{\text{NL}} = g$ as seen from Eq. (3). Note that we absorbed a factor of 1/4 into the definition of Γ_{NL} in Eq. (27b) compared to the definition of the χ_3-parameter in equation 2b of Ref. [3] to avoid any numerical pre-factors in Eq. (27). Finding the minimum gate error for each value of κ_l in Fig. 6a and plotting it as a function of $\Gamma_{\text{NL}}/\kappa_l$ shows that the error is approximately inversely proportional to $\Gamma_{\text{NL}}/\kappa_l$, see Fig. 9. We also show the results from Ref. [3] in the same plot for reference [note a rescaling of the red curve to match the definition of Γ_{NL} in Eq. (27b)]. A lower bound on the gate duration (in units of Γ_{NL}^{-1}) follows from the physical origin of the phase difference between one- and two-photon inputs. For SHG, a full Rabi oscillation between two photons in mode $\hat{b}$ and one photon in mode $\hat{c}$ is required, and this Rabi period is given by $(\pi/\sqrt{2})\Gamma_{\text{NL}}^{-1}$ (this can be seen from equations 57c and 57d in Ref. [4]). For SPM, the phase difference is simply acquired at a rate given by $2\Gamma_{\text{NL}}t$ so

the minimum required gate duration is $(\pi/2)\Gamma_{\text{NL}}^{-1}$ (this can be seen from equation 54c in Ref. [4] when accounting for the definition: $\Gamma_{\text{NL}} = \chi_3/4$). For TLEs, a bound is not as straightforwardly obtained due to the necessity of a control field to ensure the simultaneous achievement of a π phase difference and depopulating the TLE for both one- and two-photon inputs. However, Fig. 6a shows that a duration of $\sim 5\Gamma_{\text{NL}}^{-1}$ is sufficient for an error below 1%. These bounds are consistent with the relative positions of the curves in Fig. 9 and shows that using TLEs as the optical nonlinearity comes with a relative small penalty in the required loss rate of a factor of 2–3 compared to $\chi^{(2)}$ or $\chi^{(3)}$ effects.

To evaluate the potential of practical implementations, one must calculate the value of $\Gamma_{\text{NL}}/\kappa_l$. Table 1 lists numbers from the literature including each type of nonlinearity (see the supplementary materials for details on how the relevant metrics were extracted). It shows that interaction volumes achieved for SHG in $\chi^{(2)}$-materials are orders of magnitude larger than those for both SPM in $\chi^{(3)}$-materials and dipole interaction volumes[2,31–33]. The dielectric confinement mechanism employed in refs. [2,31–33] was applied to SHG in ref. [34], but more work is necessary to understand its potential for reducing the SHG interaction volume. Using $\Gamma_{\text{NL}}/\kappa_l$ as a figure of merit is not generally applicable for SHG since two optical cavity modes are involved (note that we assumed identical loss rates for all modes in ref. [4]). In the SHG literature, the conversion efficiency ($\eta_{\text{SHG}} \propto Q_b^2 Q_c$[35–37]) is often used as a figure of merit, but it appears that $\min(Q_b, Q_c)$ is the
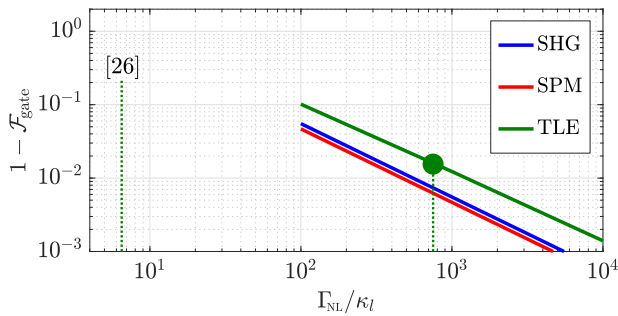

Fig. 9 Gate error as a function of the ratio between nonlinear coupling rate and linear loss rate. Calculated for the three types of nonlinearity we have studied here and in previous work. The generalized nonlinear coupling rate, Γ_{NL}, corresponds to g here and to χ_2 or $\chi_3/4$ from Ref. [4]. The vertical dotted lines show state of the art[28] and the expected performance by combining g from Ref. [28] and κ_l from Ref. [47] (green dot). Note that the figure of merit, $\Gamma_{\text{NL}}/\kappa_l$, for bulk nonlinearities are orders of magnitude smaller than for the TLE and therefore not included in this plot.

limiting factor in the quantum regime studied here. This difference in scaling of the figure of merit should be considered when designing cavities for few-photon interactions.

High confinement cavities have been realized in Si[32,33], but measurements of the SPM coupling rate are required to verify their potential. Table 1 clearly illustrates the advantage of two-level emitters compared to bulk nonlinearities in terms of the much larger nonlinear coupling rate.

DISCUSSION

In the introduction, we mentioned a few examples of two-level emitter implementations where strong coupling to an optical mode was already demonstrated. However, there has been a lot of work in recent years on other promising platforms like 1D-[38] and 2D materials[39,40]. Very strong coupling between exciton materials and plasmonic modes was also experimentally observed[41–43] and theoretical work suggested how such systems may be described by an effective Jaynes–Cummings model[44–46]. Our focus on InAs quantum dots in GaAs membranes in the previous section and Table 1 is, however, based on our assessment that they represent state-of-the-art owing to their scalability potential and excellent properties resulting from a long history of developing them as single-photon sources. Moving beyond state-of-the-art and into a parameter regime corresponding to ~1% gate error would require the nonlinear coupling rate in Ref. [28] and the linear loss rate in Ref. [47] to be achieved in the same device (illustrated with a green dot in Fig. 9). Surface passivation techniques are being used to address the challenge of achieving large Qs in GaAs cavities both with-[48] and without QDs[47]. Cavities with ultra-small dipole interaction volumes[2,31–34] also represent an interesting approach to increase g. We note, however, that with the parameters used in Fig. 6 and $g = 40$ GHz and $\omega_a = 2\pi c/940$ nm[28], the coupling-Q of mode $\hat{a}$ is $Q_C = \omega_a/\kappa_C = 530$. At the same time, $\kappa_l/g \sim 10^{-3} \Rightarrow Q_l/Q_C = 1.5 \times 10^4$ meaning that cavity mode $\hat{a}$ must be extremely over-coupled to reach the ~1% gate error regime. Further increases to g corresponds to an even smaller Q_C that could pose experimental challenges although nanobeam cavities are well-suited to reach very over-coupled regimes even at large Qs[49].

The scheme for dynamic cavity coupling originating from nonlinear mode interactions used here and in recent work[3,50–52] is compatible with a very small dipole interaction volume of the cavity mode interacting with the TLE. The control pump power may be increased to achieve the required strength of $\Lambda(t)$ as long as the overlap between the participating modes is large enough to ensure a reasonable nonlinear interaction volume. However, interference-based dynamic cavity coupling[53,54] requires the

Table 1.	Comparison of nonlinear coupling rates and linear loss rates.					
Ref.	Mat.	Type	$\frac{\Gamma_{\text{NL}}}{\text{GHz}}$	$V_{\text{int}} \left[\frac{\lambda^3}{n^3}\right]$	Q_L	$\frac{\Gamma_{\text{NL}}}{\kappa_l}$
Design proposal						
Lin2016[30]	LiNbO$_3$	$\chi^{(2)}$	0.01	1.1×10^3	2.4×10^3	1.2×10^{-4}
Minkov2019[31]	GaN	$\chi^{(2)}$	0.00021	6.7×10^4	1×10^4	9.1×10^{-6}
Choi2017[2]	Si	$\chi^{(3)}$	0.002	0.17	2×10^6	0.02
Experimental demonstration						
Lu2020[55]	LiNbO$_3$	$\chi^{(2)}$	0.0012	7.4×10^4	5.8×10^5	0.0036
Ota2018[26]	InAs	TLE	40	–	5.2×10^4	6.5
Kuruma2020[33]	InAs	TLE	4.8	–	1.6×10^5	0.8
Guha2017[29]	GaAs	–	–	–	6.0×10^6	–

The comparison is made in terms of quality factors. For each material, we specify the type of the observed nonlinearity, the absolute value of the nonlinear interaction rate, the corresponding multimode interaction volume, resonator quality factor, and the ratio between the interaction rate and resonator decay rate. Definitions of interaction volume for $\chi^{(2)}$ and $\chi^{(3)}$ nonlinearity and their relation to other parameters listed in the literature[56–61] are given in the supplementary materials.

mode to spread out across the interference paths and thereby limits how small the dipole interaction volume can be.

In conclusion, we have shown that a two-level emitter is sufficient to implement high-fidelity logical gates between photonic qubits when time-dependent control of the coupling between cavity modes and the emitter/cavity detuning is possible. Our approach represents a promising alternative to multi-level systems[17–19] by shifting complexity from the atom-like emitter to the photonic system.

Based on the demonstrated performance and potential for improvement, we consider semiconductor quantum dots to be a very promising hardware platform to implement deterministic quantum logic on photonic quantum states.

DATA AVAILABILITY
All code used to solve and optimize the control master equations is available upon request, as well as the raw output of the simulation routines.

REFERENCES
1. Knill, E., Milburn, G. & Laflamme, R. A scheme for efficient quantum computation with linear optics. *Nature* **409**, 46–52 (2001).
2. Choi, H., Heuck, M. & Englund, D. Self-similar nanocavity design with ultrasmall mode volume for single-photon nonlinearities. *Phys. Rev. Lett.* **118**, 223605 (2017).
3. Heuck, M., Jacobs, K. & Englund, D. R. Photon-photon interactions in dynamically coupled cavities. *Phys. Rev. A* **101**, 042322 (2020).
4. Heuck, M., Jacobs, K. & Englund, D. R. Controlled-phase gate using dynamically coupled cavities and optical nonlinearities. *Phys. Rev. Lett.* **124**, 160501 (2020).
5. Krastanov, S. et al. Room-temperature photonic logical qubits via second-order nonlinearities. *Nat. Commun.* **12**, 1–10 (2021).
6. Li, M. et al. Photon-photon quantum phase gate in a photonic molecule with $\chi^{(2)}$ nonlinearity. *Phys. Rev. Appl.* **13**, 044013 (2020).
7. Rauschenbeutel, A. et al. Coherent operation of a tunable quantum phase gate in cavity QED. *Phys. Rev. Lett.* **83**, 5166–5169 (1999).
8. Birnbaum, K. M. et al. Photon blockade in an optical cavity with one trapped atom. *Nature* **436**, 87–90 (2005).
9. Englund, D. et al. Controlling cavity reflectivity with a single quantum dot. *Nature* **450**, 857–861 (2007).
10. Hennessy, K. et al. Quantum nature of a strongly coupled single quantum dot-cavity system. *Nature* **445**, 896–899 (2007).
11. Rattenbacher, D. et al. Coherent coupling of single molecules to on-chip ring resonators. *N. J. Phys.* **21**, 062002 (2019).
12. Wallraff, A. et al. Strong coupling of a single photon to a superconducting qubit using circuit quantum electrodynamics. *Nature* **431**, 162–167 (2004).
13. Takahashi, H., Kassa, E., Christoforou, C. & Keller, M. Strong coupling of a single ion to an optical cavity. *Phys. Rev. Lett.* **124**, 013602 (2020).
14. Ralph, T. C., Söllner, I., Mahmoodian, S., White, A. G. & Lodahl, P. Photon sorting, efficient bell measurements, and a deterministic controlled-Z gate using a passive two-level nonlinearity. *Phys. Rev. Lett.* **114**, 173603 (2015).
15. Nysteen, A., McCutcheon, D. P. S., Heuck, M., Mørk, J. & Englund, D. R. Limitations of two-level emitters as nonlinearities in two-photon controlled-PHASE gates. *Phys. Rev. A* **95**, 1–7 (2017).
16. Yang, F., Lund, M. M., Pohl, T., Lodahl, P. & Mølmer, K. Deterministic photon sorting in waveguide QED systems. *Phys. Rev. Lett.* **128**, 213603 (2022).
17. Duan, L.-M. & Kimble, H. J. Scalable photonic quantum computation through cavity-assisted interactions. *Phys. Rev. Lett.* **92**, 127902 (2004).
18. Johne, R. & Fiore, A. Proposal for a two-qubit quantum phase gate for quantum photonic integrated circuits. *Phys. Rev. A—At. Mol. Opt. Phys.* **86**, 1–5 (2012).
19. Iakoupov, I., Borregaard, J. & Sørensen, A. S. Controlled-phase gate for photons based on stationary light. *Phys. Rev. Lett.* **120**, 010502 (2018).
20. McCutcheon, M. W., Chang, D. E., Zhang, Y., Lukin, M. D. & Lončar, M. Broadband frequency conversion and shaping of single photons emitted from a nonlinear cavity. *Opt. Express* **17**, 22689–22703 (2009).
21. Choi, H., Zhu, D., Yoon, Y. & Englund, D. Cascaded cavities boost the indistinguishability of imperfect quantum emitters. *Phys. Rev. Lett.* **122**, 183602 (2019).
22. Nielsen, M. A. & Chuang, I. L. *Quantum Computation and Quantum Information: 10th Anniversary Edition* 10th edn (Cambridge University Press, 2011).

23. Bezanson, J., Edelman, A., Karpinski, S. & Shah, V. B. Julia: a fresh approach to numerical computing. *SIAM Rev.* **59**, 65–98 (2017).
24. Mogensen, P. K. & Riseth, A. N. Optim: a mathematical optimization package for julia. *J. Open Source Softw.* **3**, 615 (2018).
25. Lodahl, P., Mahmoodian, S. & Stobbe, S. Interfacing single photons and single quantum dots with photonic nanostructures. *Rev. Mod. Phys.* **87**, 347–400 (2015).
26. Jacobs, K. *Stochastic Processes for Physicists: Understanding Noisy Systems* (Cambridge University Press, 2010).
27. Jacobs, K. *Quantum Measurement Theory and its Applications* (Cambridge University Press, 2014).
28. Ota, Y. et al. Large vacuum rabi splitting between a single quantum dot and an h0 photonic crystal nanocavity. *Appl. Phys. Lett.* **112**, 093101 (2018).
29. Supradeepa, V., Huang, C.-B., Leaird, D. E. & Weiner, A. M. Femtosecond pulse shaping in two dimensions: towards higher complexity optical waveforms. *Opt. Express* **16**, 11878–11887 (2008).
30. Weiner, A. M. Ultrafast optical pulse shaping: a tutorial review. *Opt. Commun.* **284**, 3669–3692 (2011).
31. Hu, S. & Weiss, S. M. Design of photonic crystal cavities for extreme light concentration. *ACS Photonics* **3**, 1647–1653 (2016).
32. Hu, S. et al. Experimental realization of deep subwavelength confinement in dielectric optical resonators. *Sci. Adv.* **4**, eaat2355 (2018).
33. Albrechtsen, M. et al. Nanometer-scale photon confinement inside dielectrics. Preprint at https://arxiv.org/abs/2108.01681 (2021).
34. Ateshian, L., Choi, H., Heuck, M. & Englund, D. Terahertz light sources by electronic-oscillator-driven second harmonic generation in extreme-confinement cavities. Preprint at https://doi.org/10.1364/CLEO_SI.2021.SW2K.1 (2021).
35. Buckley, S. et al. Multimode nanobeam cavities for nonlinear optics: high quality resonances separated by an octave. *Opt. Express* **22**, 26498–26509 (2014).
36. Lin, Z., Liang, X., Lončar, M., Johnson, S. G. & Rodriguez, A. W. Cavity-enhanced second-harmonic generation via nonlinear-overlap optimization. *Optica* **3**, 233–238 (2016).
37. Minkov, M., Gerace, D. & Fan, S. Doubly resonant $\chi^{(2)}$ nonlinear photonic crystal cavity based on a bound state in the continuum. *Optica* **6**, 1039–1045 (2019).
38. He, X. et al. Carbon nanotubes as emerging quantum-light sources. *Nat. Mater.* **17**, 663–670 (2018).
39. Toth, M. & Aharonovich, I. Single photon sources in atomically thin materials. *Annu. Rev. Phys. Chem.* **70**, 123–142 (2019).
40. Azzam, S. I., Parto, K. & Moody, G. Prospects and challenges of quantum emitters in 2d materials. *Appl. Phys. Lett.* **118**, 240502 (2021).
41. Wen, J. et al. Room-temperature strong light-matter interaction with active control in single plasmonic nanorod coupled with two-dimensional atomic crystals. *Nano Lett.* **17**, 4689–4697 (2017).
42. Geisler, M. et al. Single-crystalline gold nanodisks on ws2 mono- and multilayers for strong coupling at room temperature. *ACS Photonics* **6**, 994–1001 (2019).
43. Qin, J. et al. Revealing strong plasmon-exciton coupling between nanogap resonators and two-dimensional semiconductors at ambient conditions. *Phys. Rev. Lett.* **124**, 063902 (2020).
44. Tserkezis, C. et al. On the applicability of quantum-optical concepts in strong-coupling nanophotonics. *Rep. Prog. Phys.* **83**, 082401 (2020).
45. Denning, E. V., Wubs, M., Stenger, N., Mørk, J. & Kristensen, P. T. Cavity-induced exciton localization and polariton blockade in two-dimensional semiconductors coupled to an electromagnetic resonator. *Phys. Rev. Res.* **4**, L012020 (2022).
46. Denning, E. V., Wubs, M., Stenger, N., Mørk, J. & Kristensen, P. T. Quantum theory of two-dimensional materials coupled to electromagnetic resonators. *Phys. Rev. B* **105**, 085306 (2022).
47. Guha, B. et al. Surface-enhanced gallium arsenide photonic resonator with quality factor of 6×10^6. *Optica* **4**, 218–221 (2017).
48. Kuruma, K., Ota, Y., Kakuda, M., Iwamoto, S. & Arakawa, Y. Surface-passivated high-q gaas photonic crystal nanocavity with quantum dots. *APL Photonics* **5**, 046106 (2020).
49. Quan, Q., Deotare, P. B. & Loncar, M. Photonic crystal nanobeam cavity strongly coupled to the feeding waveguide. *Appl. Phys. Lett.* **96**, 203102 (2010).
50. Reddy, D. V. & Raymer, M. G. Photonic temporal-mode multiplexing by quantum frequency conversion in a dichroic-finesse cavity. *Opt. Express* **26**, 28091–28103 (2018).
51. Heuck, M. et al. Unidirectional frequency conversion in microring resonators for on-chip frequency-multiplexed single-photon sources. *N. J. Phys.* **21**, 1–19 (2018).
52. Zhang, M. et al. Electronically programmable photonic molecule. *Nat. Photonics* **13**, 36–40 (2019).
53. Tanaka, Y. et al. Dynamic control of the Q factor in a photonic crystal nanocavity. *Nat. Mater.* **6**, 862–865 (2007).
54. Xu, Q., Dong, P. & Lipson, M. Breaking the delay-bandwidth limit in a photonic structure. *Nat. Phys.* **3**, 406–410 (2007).

55. Lu, J., Li, M., Zou, C.-L., Sayem, A. A. & Tang, H. X. Toward 1% single-photon anharmonicity with periodically poled lithium niobate microring resonators. *Optica* **7**, 1654–1659 (2020).
56. Rodriguez, A., Soljačić, M., Joannopoulos, J. D. & Johnson, S. G. χ(2) and χ(3) harmonic generation at a critical power in inhomogeneous doubly resonant cavities. *Opt. Express* **15**, 7303–7318 (2007).
57. Sipe, J. E., Bhat, N. A. R., Chak, P. & Pereira, S. Effective field theory for the nonlinear optical properties of photonic crystals. *Phys. Rev. E* **69**, 016604 (2004).
58. Bhat, N. A. R. & Sipe, J. E. Hamiltonian treatment of the electromagnetic field in dispersive and absorptive structured media. *Phys. Rev. A* **73**, 063808 (2006).
59. Quesada, N. & Sipe, J. E. Why you should not use the electric field to quantize in nonlinear optics. *Opt. Lett.* **42**, 3443–3446 (2017).
60. Sanford, N. A. et al. Measurement of second order susceptibilities of gan and algan. *J. Appl. Phys.* **97**, 053512 (2005).
61. Notomi, M. Manipulating light with strongly modulated photonic crystals. *Rep. Prog. Phys.* **73**, 096501 (2010).

AUTHOR CONTRIBUTIONS

The control protocol was conceived by the authors through joint discussions. The detailed protocol simulation, optimization, and analysis were worked out by M.H. with help from S.K. The final manuscript was vetted by all authors.

COMPETING INTERESTS

The authors declare no competing interests.

ADDITIONAL INFORMATION

Supplementary information The online version contains supplementary material available at https://doi.org/10.1038/s41534-022-00604-5.

Correspondence and requests for materials should be addressed to Stefan Krastanov or Mikkel Heuck.

Reprints and permission information is available at http://www.nature.com/reprints

Publisher's note Springer Nature remains neutral with regard to jurisdictional claims in published maps and institutional affiliations.